

The SELEX Phototube RICH Detector

J. Engelfried ^{a,1}, I. Filimonov ^{c,2}, J. Kilmer ^a, A. Kozhevnikov ^b,
V. Kubarovsky ^b, V. Molchanov ^b, A. Nemitkin ^c, E. Ramberg ^a,
V. Rud ^c, L. Stutte ^a

^a*Fermi National Accelerator Laboratory, Batavia, IL, USA*³

^b*Institute for High Energy Physics, Serpukhov, Russia*⁴

^c*Moscow State University, Moscow, Russia*⁴

Abstract

In this article, construction, operation, and performance of the RICH detector of Fermilab experiment 781 (SELEX) are described. The detector utilizes a matrix of 2848 phototubes for the photocathode to detect Cherenkov photons generated in a 10 m Neon radiator. For the central region an N_0 of 104 cm^{-1} , corresponding to 13.6 hits on a $\beta = 1$ ring, was obtained. The ring radius resolution measured is 1.6%.

1 Introduction

The Fermilab experiment E781 (SELEX): A Segmented Large x_F Baryon Spectrometer [1,2], which took data in the 1996/97 fixed target run at Fermilab, is designed to perform high statistics studies of production mechanisms and decay physics of charmed baryons such as Σ_c , Ξ_c , Ω_c and Λ_c . The physics goals of the experiment require good charged particle identification to look for the different baryon decay modes. One must be able to separate π , K and p over a wide momentum range when looking for charmed baryon decays like $\Lambda_c^+ \rightarrow p K^- \pi^+$.

¹ Now at Instituto de Física, Universidad Autonoma de San Luis Potosí, Mexico

² deceased

³ Work supported by the US Department of Energy under contract NO. DE-AC02-76CHO3000.

⁴ Supported by the Russian Ministry of Science and Technology.

A RICH [3] detector with a 2848 phototube photocathode array has been constructed [4,5] to do this. The detector begins about 16 m downstream of the charm production target, with two analysis magnets with 800 MeV/c p_t -kick each in-between, and is surrounded by multi-wire proportional and drift chambers which provide particle tracking. The average number of tracks reaching the RICH is about 5 per event. First results from this detector can be found in [6].

In this article we first describe the properties of the main parts of the detector (vessel, mirrors, photon detector). Finally we report about stability during the run, performance, and some preliminary physics results.

2 Vessel

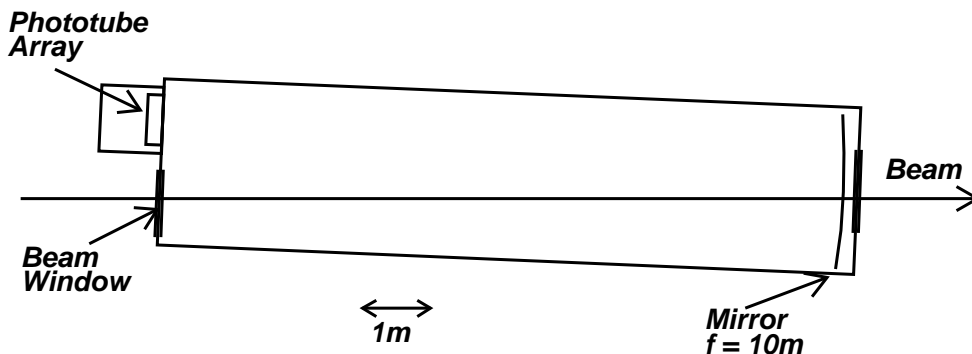


Fig. 1. Vessel Layout.

The E781 RICH vessel is a low carbon steel vessel 10.22 m in length, 93 in. in diameter and with a wall thickness of $\frac{1}{2}$ in. The end flanges are 1.5 in. thick aluminum with provisions for thin beam windows and a phototube holder plate to be described later. The heavy construction⁵ allowed the vessel to be leak checked with a helium mass spectrometer. The vessel specification was to show no leak greater than 10^{-9} atm cc/s. It easily passed the leak test and proved to be a very tight vessel in operation.

The vessel has three feedthroughs and several piping connections for the gas system. Electrical feedthroughs are gas-tight vacuum coaxial connectors. Provisions were made for thermistors for both ends of the vessel to monitor internal temperature and an LED pulser test array to supply calibration signals for the phototubes. The third port has connections for the gas analyzers.

⁵ Rode Welding Service Inc., Elk Grove Village, IL.

The entire interior of the vessel was painted with a flat black paint to reduce reflections of photons in the vessel. To keep the paint from contaminating the radiator gas a very low out-gassing paint⁶ was chosen [7]. The inner surface of the vessel was sand-blasted before painting and then sprayed.

Several other mechanical features of the vessel are significant. The vessel is tilted off the horizontal axis by 2.4 deg with the beam entering horizontally through a thin window. The RICH is also mounted on a rail system that allows it to be moved out of the beam line for the alignment of the mirrors and for certain types of physics running. Stops on the rails were adjusted to allow the vessel to be put back on the beam line repeatably within ± 1 mm after a vessel move.

The entrance and exit windows are fabricated⁷ from a 3-layer laminate that consists of 3 mil Kevlar[®] cloth, 1 mil aluminum foil and 1.5 mil charcoal Tedlar[®]. These three elements combined give a strong, gas-tight and light-tight barrier. Permeability tests were conducted with both air and neon gas samples, and showed results consistent with the background level of the measuring apparatus. Light-tightness was checked by measuring the noise rate in a phototube placed in a box with one side made of the window fabric, and showed no observable increase from that of a phototube inside a light-tight box. For mounting on the vessel, the window material was sandwiched between two mylar rings, and inserted between two aluminum rings which were bolted together along with a rubber o-ring seal.

To avoid the construction of a complicated gas-filling system to prevent the collapse of the phototube holder plate, which can only support a pressure difference across it of 3 psid, a new gas system was constructed to purge the vessel which requires only an operating pressure of 1 psig [8]. The vessel was purged by flow purging from air to carbon dioxide. Carbon dioxide was introduced at the bottom of the vessel and displaced air was removed from the top. After the air was removed a separate circuit of the system added neon to the now CO₂ filled vessel and froze out the excess CO₂ with a liquid nitrogen cooled freezer keeping the pressure constant. When the vessel contained neon with only a trace of CO₂ the final step was to pump the vessel gas through a liquid nitrogen cooled adsorber to remove the last traces of contaminates. In the initial purge for the run the oxygen background was reduced to 3 ppm. The oxygen level was data logged throughout the run. Over the course of a running period lasting more than a year the oxygen level rose to an estimated (20 ± 12) ppm. The large error in the final O₂ level stems from the fact that the oxygen monitor failed in the middle of the run due to aging; replacing the

⁶ Lord Corporation Industrial Coatings, Aeroglaze Z306 polyurethane flat black paint.

⁷ Shelldall, Northfield, MN.

cell after the run introduced some oxygen into the system and resulted in a reading of 32 ppm O₂. An extrapolation from the last accurate reading was 8 ppm.

The gas system was designed to allow the removal of oxygen from the neon gas during a running period. Because of the tightness of the vessel and gas system the oxygen contamination never became severe enough to require purifying the neon. As a result the initial gas charge remained without change in the vessel for the entire run.

The vessel also has a constant temperature control system provided by a water coil around the vessel wall and a chilled water system. Fifteen cm thick building insulation was used to help keep the vessel temperature constant. During the running period the temperature was set to the same temperature as when the mirror mounts were glued onto the mirrors and the mirrors were installed and aligned. Over the course of the run (15 months) the temperature was $21.5\text{ }^{\circ}\text{C} \pm 1.5\text{ }^{\circ}\text{C}$.

To monitor the status of the detector, data was logged [9] for the entire run once per minute. Parameters monitored were: atmospheric pressure, vessel pressure, vessel temperature, oxygen content, temperature at several locations within the phototube box, temperature in the digitizer crates, voltages at the end of the HV Zener diode chains, and status of the low voltage system. Error conditions were automatically checked and reported to the shift crew.

3 Mirrors

The mirror plane at the end of the vessel is build up of 16 hexagonally shaped spherical mirrors, covering a total area of $2.4\text{ m} \times 1.2\text{ m}$, as shown in Fig. 2. Each mirror is 40 cm across (46 cm tip-to-tip), has a thickness of 10 mm, and is made of low expansion glass⁸. The average radius of the mirrors is 1980 cm, with a deviation of $< 5\text{ cm}$ RMS between mirrors as well as on one mirror. The mirrors were polished⁹ until the image of a point source illuminating the whole mirror was $< 1\text{ mm}$. The back of the mirror is rough polished to the same radius.

The leftmost and the rightmost mirrors in the central row had to be truncated by 3 in. to fit into the vessel. The central mirror has a cutout of $6.8\text{ cm} \times 11\text{ cm}$ to allow non-interacting beam particles to pass through the detector without interacting in the mirror to reduce bad effects in more downstream detectors.

⁸ Schott Tempax Glass, provided by Abrisa Industrial Glass Inc., Venture, CA.

⁹ Astronomically Xenogenic Enterprises (AXE), Tucson, AR.

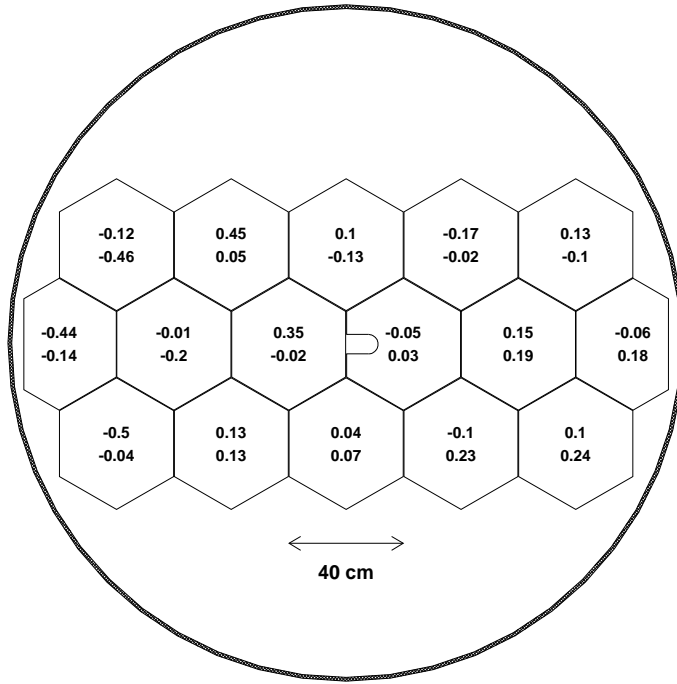


Fig. 2. Mirror Layout in the Vessel. The numbers show the deviation from the average center of curvature for the horizontal (top) and vertical (bottom) coordinate in cm.

The mirrors were coated¹⁰ with Aluminum, and an overcoating of MgF₂. The reflectivity was > 85% at 160 nm.

The sphericity of all mirrors was measured using the Ronchi method [10], which confirmed that the mirrors were produced within the specifications. The results were used to mount the mirrors with the best sphericity in the center, and to have a minimal difference of the average radius between neighboring mirrors.

The mirrors are fixed individually to a flat, low mass honeycomb panel¹¹ of 1 in. thickness with a 3 point kinematic mount (see Fig. 3). Each mount consists of an aluminum pad glued¹² to the back of the mirror, a ball bearing, and a double differential screw built out of a $\frac{1}{4}$ in. diameter titanium rod with a thread of 80/in., a $\frac{1}{2}$ in. aluminum cylinder with a thread of 13/in. and a nylon cylinder of 1 in. diameter. This mounting scheme allowed alignment of the mirrors on a sphere with a maximum sagitta of 2 cm, while still maintaining an angular accuracy of 50 μ rad.

¹⁰ Acton Research Corporation, Acton, MA.

¹¹ Plascore Inc., Zeeland, MI.

¹² BIPAX[®] TRA-BOND BA-2151, TRA-CON, Medford, MA.

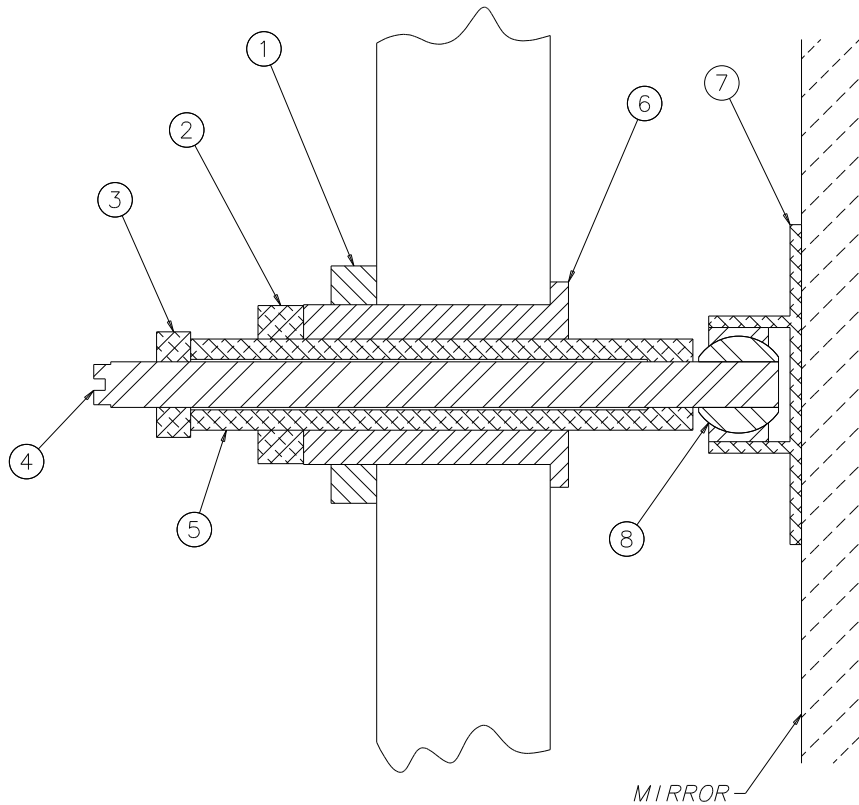


Fig. 3. Mirror Mount. The honeycomb panel is 1 in. thick. 1: Nylon nut. 2,3: Aluminum nuts. 4: Titanium rod. 5: Aluminum rod. 6: Nylon cylinder. 7: Aluminum pad glued to mirror. 8: Ball bearing.

Due to space restrictions in the experimental area, the mirrors had to be mounted and aligned with the vessel moved laterally by 3 m from its final location in the experiment. Great care was taken in assuring that vibrations during movement of the vessel do not misalign the mirrors. After mounting the mirrors on the honeycomb panel, a first rough alignment was done by eye. The final alignment was performed with a laser mounted on a theodolite base, sited at the average center of curvature. The mirror angles were adjusted until the reflected spot observed back at the center of curvature had no more than 2 mm displacement.

To determine the alignment of the mirrors during the run, standard experiment data (no special data sets are needed) were used to measure the center of curvature of each mirror. In an iterative procedure the predicted ring centers (using the previous set of constants) are compared to the centers obtained from a circle fit to isolated rings, using only tracks where the Cherenkov light was reflected by one mirror. This procedure converges after typically 5 iterations. With a typical data set of 1 million events, between 2000 and 50000 tracks are used to align the different mirrors. This alignment procedure was repeated for data sets taken over the whole running time of the experiment and it

was found that the obtained results are constant. The final deviations from an average center of curvature are shown in Fig. 2. The mean lateral displacement is 2.6 mm.

4 Photodetector

4.1 Holder plate

The phototube holder plate is made¹³ from a 55 in. wide, 27 in. high, 3 in. thick aluminum block. Figure 4 shows a cross section of a few of the 2848 (89×32) hexagonally packed (0.635 in. spacing) holes of approximately 0.6 in. diameter that were drilled through it.

One side of each hole is a straight channel 2 in. in depth, which is used to support a phototube. A quartz window¹⁴ of 2 mm thickness was inserted into this side of the hole and glued in place, providing a gas seal between the neon radiator and the phototube housing. After the windows were glued in place, they were checked for gas-tightness using a helium leak detector. A small number of leaky ($> 10^{-8}$ atm cc/s) windows were replaced. All windows were then cleaned of residual glue (which was not UV transparent) and their transmission checked using a spectrophotometer equipped with a fiber-optic system interface.

The other side of each hole is a tapered channel 1 in. in depth, with an inner radius of 0.4 in. An aluminized mylar cone is inserted into this side and extends slightly out from the block in order to give essentially 100% coverage for photon detection. The 0.4 in. inner radius of the cone section of the hole was made to be the same size as the photocathode of the phototubes. In order to center the tubes on the aperture and provide enough friction to hold them snugly in place, thin Velcro[®] strips (loop half) were affixed along each tube. To minimize the loss of UV photons, the gap between the quartz window and the phototube had to be kept as small as possible. The FEU60 phototubes however were coated with PTP wavelength shifter, so a small gap was needed in order to avoid removing the coating. These two goals were achieved by placing a thin (3 mil) mylar ring of inner diameter 0.4 in. up against the window.

¹³ Walco Tool and Engineering Corp., Lockport, IL.

¹⁴ Suprasil 2 from Heraeus Amersil Inc., Duluth, GA.

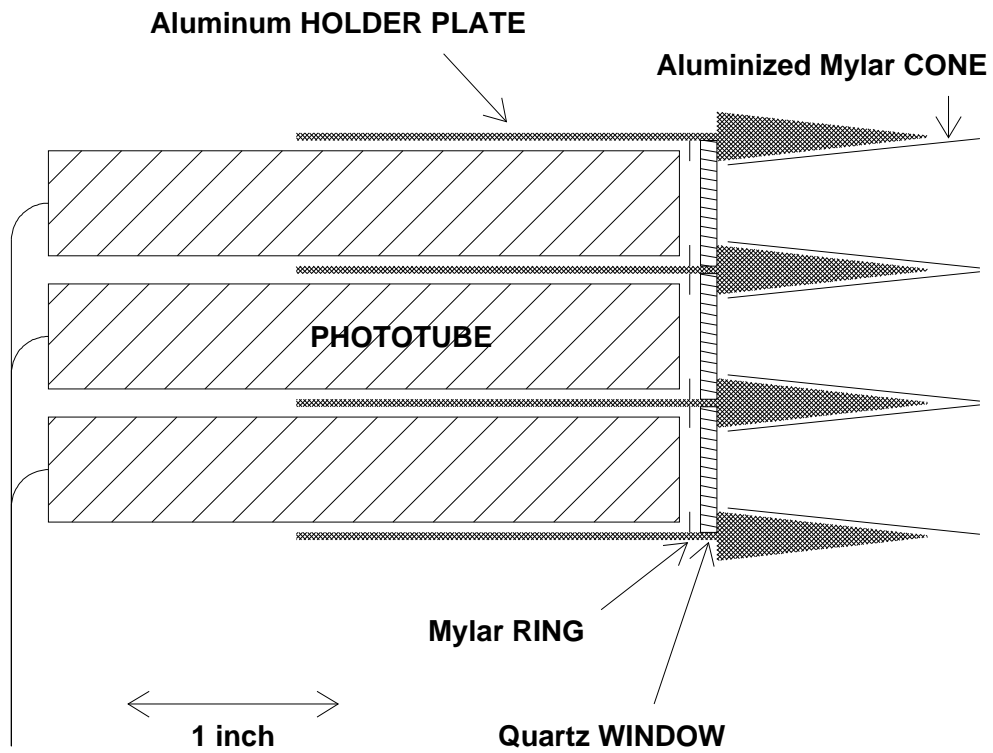
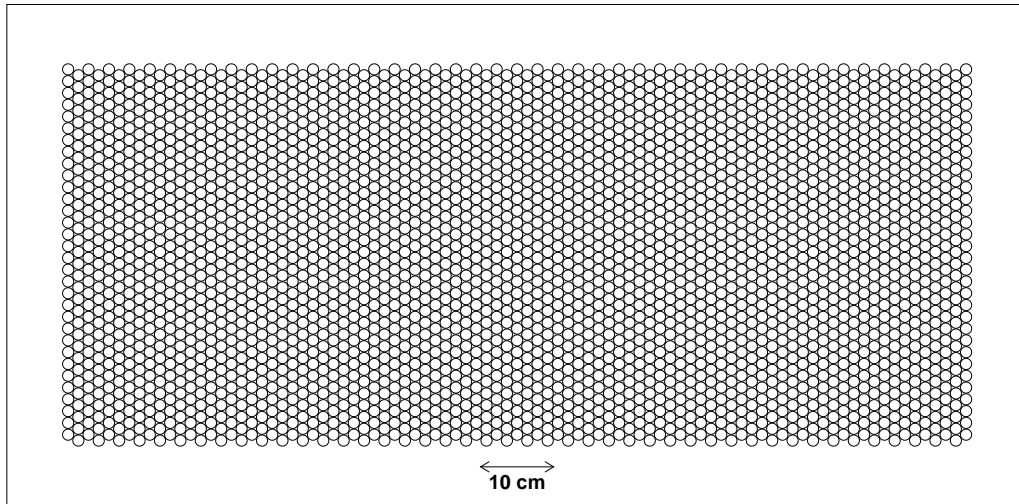


Fig. 4. Front view (top) and partial cross section (bottom) through the Phototube Holder Plate.

4.2 Phototubes

Two different types of $\frac{1}{2}$ in. diameter, 10 mm bi-alkali photocathode, 10-stage tubes are used. The first is a commercially available tube R760¹⁵ which has a quartz window and thus response down to 170 nm. It has a quantum efficiency of approximately 25 % at its peak wavelength of 350 nm. The second is a Russian tube (FEU60) which has a glass entrance window. These tubes were coated with PTP wavelength shifter to reach the same wavelength range as the R760 tubes (the quartz entrance window of the holder plate provided the 170 nm wavelength cutoff). Initial tests in a vacuum reflectometer equipped with a Deuterium VUV-UV light source showed that the thickness of the PTP was not a critical parameter for their performance, so as many as 70 tubes were coated at one time in a vacuum deposition jar.

Each of the phototubes in the SELEX RICH differed with respect to their performance under high voltage. Because each column of 32 phototubes was connected to a single high voltage, it was thus required to determine each phototube's characteristics and match it to 31 other similar tubes.

The two types of tubes, R760 and FEU60, are dramatically different in their quantum efficiency (Q.E.) and noise characteristics. The FEU60 tubes are on average only 42 % as efficient and have at least an order of magnitude greater noise at operating voltage than the R760 tubes. Because it was desired to limit the accidental noise in the detector to less than 0.5 %, a simple algorithm was developed to determine operating voltage: either the voltage where the Q.E. plateaued, or the voltage where the tube's inherent noise reached 30 kHz. This would limit noise in the detector up to our specification for gate values up to 170 ns.

The operating parameters of the phototubes were determined with a test setup where 32 phototubes could be measured at once. Quantum efficiencies were measured relative to a standard R760 phototube, whose absolute Q.E. was only approximately known. The setup used a blue LED, whose light was delivered to 32 identical phototube holders and the standard tube via optical fibers, all inside a dark box. The LED was driven such that it delivered on the order of 5 % of a photoelectron per pulse to each phototube. The output of the phototubes were digitized with the hybrid chips used in the detector, and the ECL output coming from this readout was sent to two CAMAC scalers in series. One scaler was gated for 100 ns in time with the signals corresponding to the LED light. The other scaler was gated for the same amount of time, but midway between successive LED pulses, to monitor the inherent noise of the phototube. This noise level was subtracted from the

¹⁵Hamamatsu Corp., Bridgewater, NJ.

in-time scaler count to provide the true in-time response of the phototube. Another scaler kept count of the number of LED pulses to provide a normalization. The phototube voltage for all 32 test tubes was provided by a CAMAC-controlled high voltage supply¹⁶ and was scanned over the operating voltage range for all tubes. Approximately $5 \cdot 10^5$ LED pulses were taken for each data point.

After testing all phototubes, a computerized matching program was developed to associate 34 phototubes having the same characteristics into a single batch with one operating point for high voltage. Two phototubes were kept as spares and the remaining 32 were bundled together in two batches for installation in the detector. In the central part of the phototube holder plate the R760 and the FEU60 tubes were installed in alternating columns; 19 columns are equipped with R760 tubes. In the outer parts, only FEU60 tubes were installed.

4.3 High Voltage, Low Voltage, and Readout Systems

To accommodate the wide range of operating voltages for the phototubes (FEU60: 1300 V to 1900 V with a current of $\approx 150 \mu\text{A}$ per tube, R760: 900 V to 1250 V with a current draw of $\approx 300 \mu\text{A}$ per tube) and the large number of tubes, six chains of air-cooled Zener diodes were used, each driven by a high voltage power supply¹⁷ delivering 100 mA. The voltage for one of the 89 columns is selected at the proper location within the Zener diode chains. This distribution system is located outside the phototube box (Fig. 5). Inside the box, the cables are soldered together with the wires to each of the 32 phototubes on a small fanout board. The ground returns are collected as well via fanout boards and are connected in common to a feedthrough panel. A support system holds the fanout boards in place.

An interlock system is used so that the high voltage is shut off before the cover can be removed from the phototube box. Four separate rocker switches (one at each corner of the box) will detect whether or not the box is closed. In addition, signals from several temperature sensors located inside the box to detect any unusual conditions contribute to the interlock.

About 1 kW of heat is generated inside the box by the phototubes. A simple cooling system was designed to remove the heat using chilled water with a light-tight heat exchanger. The cooled air enters through a long slit in the bottom of the box near the phototubes. There are two returns for the air,

¹⁶ LeCroy Corp., Chestnut Ridge, NY. Model 4032

¹⁷ Manufactured in Russia.

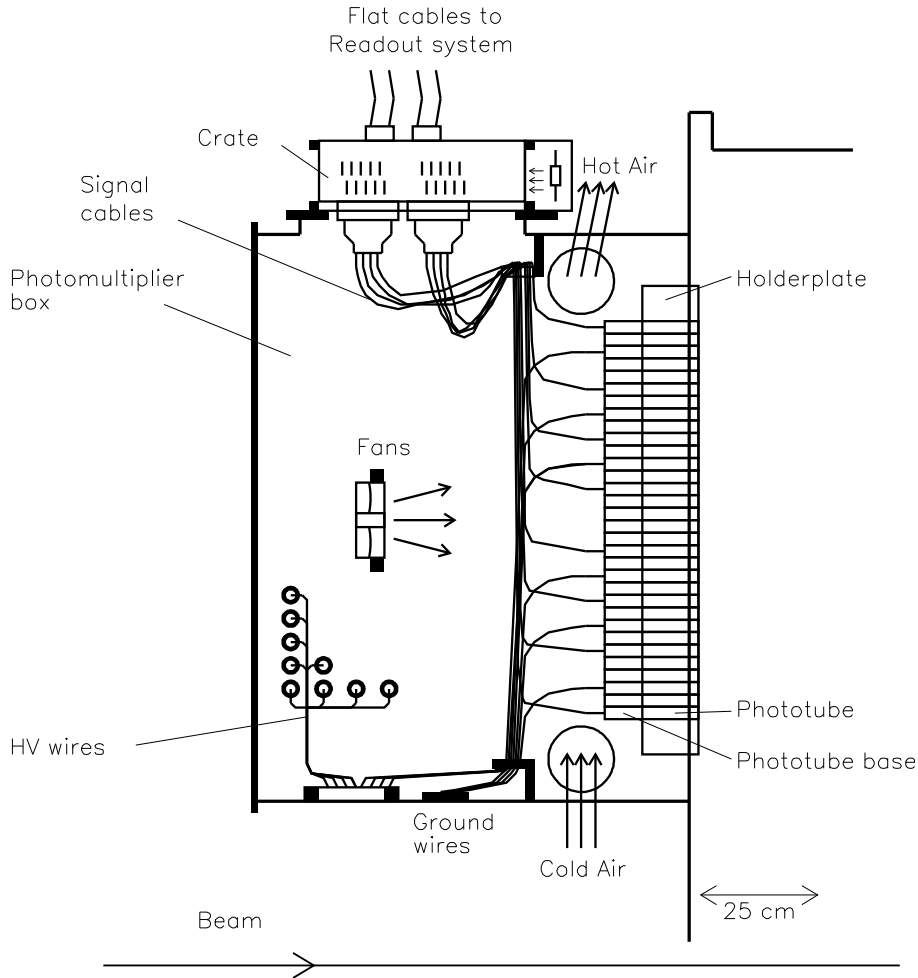


Fig. 5. Phototube Box.

each located near the top sides of the box. Fans are located inside the box to improve the airflow.

The phototubes are grouped in sets of 16, two sets comprising a column of 32 phototubes in the 89×32 matrix. The output signals from a group of 16 phototubes are soldered onto paddle cards. These cards contain a $1\text{ k}\Omega$ resistor for each channel which protects the corresponding readout chip from charge build-up whenever the paddle cards are initially connected. The paddle cards plug into a lighttight backplane of one of three custom made crates, located on top of the phototube box (Fig. 5). 96-pin Eurocard connectors¹⁸ are used in the backplanes. To prevent cross talk between the signal wires, only every third column in the connector is used, alternating the signal and ground pins; all unused pins are grounded.

¹⁸ AMP Inc., Harrisburg, PA. Type 1-215913-4.

The readout electronics, mounted on cards in the crates, consists of hybrid chips¹⁹ containing a preamplifier, a discriminator and an ECL line driver. The $\pm 6\text{ V}$ operating voltages for the chips are provided by six power supplies²⁰ and distributed to the cards via the backplane with highcurrent connectors²¹. Fans are mounted on each crate for cooling the hybrid chips. Air flow sensors are located in the air stream for each crate to monitor this cooling and to provide a safety switch-off.

During the initial phase of installation of the hybrid chip readout, the cooling system was not adequate to keep the chips at a modest temperature. During the run many chips stopped working. An analysis of these chips indicated equal failures of the amplifier and discriminator. Although the cooling system was improved, chips continued to fail at the rate of several per week. Spare chips were used to replace failed chips on the cards. However, the population of these spare chips was not adequate to deal with the chip failure rate. An alternative readout card was developed that could be plugged into the same electronics infrastructure and that delivered the same type of output. This card consisted of a preamplifier circuit board with discrete components, leading into a Nanometrics N277²² discriminator and ECL driver card. These cards replaced 32 channels at a time and freed up hybrid chips. At the end of the run, about 1/4 of the channels were serviced by N277 cards.

The 40 ns wide digital outputs from the hybrid chips and the N277 cards are routed to ECL Latches [11], which were actually 1 bit shift registers for every channel. The shifting is performed every 57 ns ($\frac{1}{3}$ of the Tevatron radio frequency). 3 slices were combined for a total integration time of 170 ns. No attempt was made to shorten the integration time, since the detector showed a very low noise rate. The zero suppressed readout yielded only the addresses of hit channels.

4.4 LED Monitoring System

The LED monitoring system was implemented for off-spill monitoring and checks of the photocathode and readout. This system illuminates the photocathode surface with short light pulses from blue LEDs mounted onto the mirror support frame. It also includes LED driver circuits (to ensure short light pulses), separate for each LED, fed from a 12 VDC power supply, and a pulse generator.

¹⁹ Designed by Moscow State University. Manufactured in Russia and Hybrids International, Ltd, Olathe, KS.

²⁰ Lambda Electronics Inc., Melville, NY. LXS-7-6-OV (60 A).

²¹ AMP Inc., Harrisburg, PA. Types 207541-3 and 207609-3.

²² Nanometric Systems Inc., Oak Park, IL.

The LED drivers are connected in four chains, about 10 LEDs in each. Only two chains are used, the others are spare. The whole chain is fired simultaneously from a NIM pulse generator either manually, or by computer control. The amount of light produced by the LEDs can be controlled via the pulse amplitude manually. The distance between LEDs and photocathode is rather big (the vessel length), giving a very even distribution of light on the photocathode surface. Short pulses give about the same phototube response as Cherenkov light, so the monitoring conditions are very close to the working ones.

An interspill monitoring task ran automatically during the whole run and produced a list of "hot" and not working channels. To determine noise, a readout was initiated without firing the LEDs. Dead and hot channels were stored in a database and are used in the offline analysis to adjust parameters used in the likelihood function (see later).

5 Determination of Performance Parameters

In this section we define and determine the operation and performance parameters of the detector. After a description of the particle identification algorithm, we determine the Figure of Merit N_0 , the refractive index, the single hit resolution σ_h , and the ring radius resolution σ_r , as a function of time (where needed).

5.1 Particle Identification Method

Figure 6 is a single event display which demonstrates the low noise of the detector (average 6 hits for beam off events) and its clear multi-track capability. This event has a 600 GeV/c Σ^- interaction, producing a 380 GeV/c Λ_c^+ , which decayed after 2.2 cm into a 154 GeV/c proton (track 4), a 152 GeV/c K^- (track 6), and a 74 GeV/c π^+ (track 5). All three decay tracks are identified in the RICH detector.

A maximum likelihood analysis [14] is performed for each track in the event. The algorithm uses tracking information to determine the ring centers and then examines hypotheses for several different particle types for each track. The likelihood function compares the number of seen hits to the expected number, using measured efficiencies (N_0), single hit resolutions, and the track momentum, for every hypothesis. The expected background is calculated for every track separately counting hits in a band outside the radius for a $\beta = 1$ particle; this method is used because it automatically takes into account over-

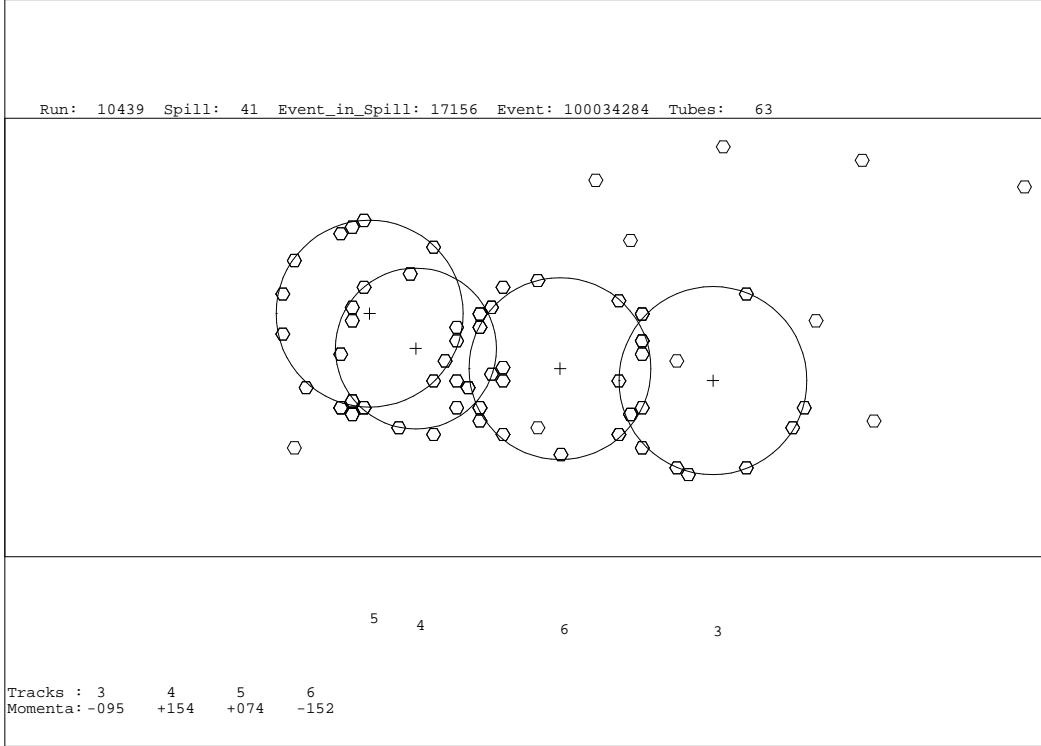


Fig. 6. Single Event Display. The small hexagons represent a hit phototube, the circle show the ring for the most probable hypothesis, the numbers below the rings denote the track numbers.

lapping rings. To discriminate between different particles, a cut is used on the ratio of likelihoods for different hypotheses. This method works for all hypotheses, even those below threshold.

5.2 Determination of N_0

One measure of the response of a Cherenkov counter is the Figure of Merit N_0 , which is defined by the relation [12] $N_0 = N/(L \sin^2 \theta)$, where N is the number of detected photons, L is the radiator length and θ is the Cherenkov angle. The photodetector has three separate regions: the central, high momentum section and the two outer, low momentum sections, so three different N_0 's must be calculated. In addition, one of the central mirrors has a section removed where the non-interacting 600 GeV/c beam tracks passed, so another N_0 is needed to describe this region. Because it is desirable to measure N_0 throughout the run, standard interaction data are used, with cuts applied to select tracks that are well-isolated and have all of their photons in the region of interest. Figure 7 shows N_0 vs time over the course of the run for two representative regions of the detector: the central region (Average $N_0 = 108.3 \text{ cm}^{-1}$) and one of the side regions (Average $N_0 = 69.7 \text{ cm}^{-1}$). Apart from the first three data

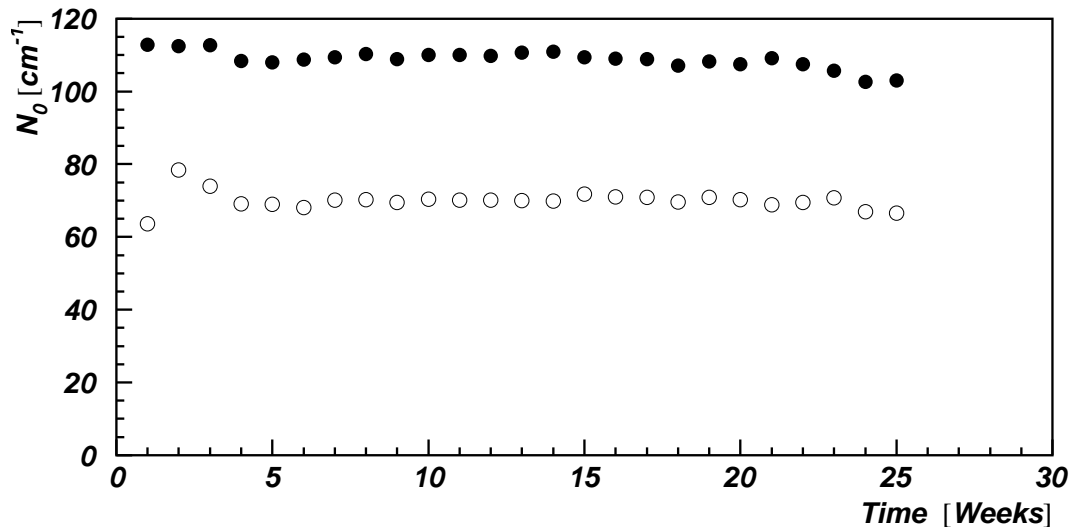


Fig. 7. N_0 for Center and West Region versus Time.

sets, which had limited statistics, N_0 is seen to vary by less than 6% over the course of the run. After correcting for the number of dead and noisy channels observed, N_0 is constant to 2.5% as a function of time. Table 1 gives the average uncorrected N_0 as a function of region. Even though the Hole region

Region	N_0 [cm^{-1}]
Positive	69.7
Central	108.3
Hole	75.6
Negative	71.4

Table 1

N_0 for different detector regions.

has an N_0 which is similar to that of the side regions, only a small number of tracks populate it so that the average N_0 over all tracks in the Central region is 104 cm^{-1} .

5.3 Determination of the refractive index

Determining the index of refraction of the gas n , or as done here $(n - 1)$, as a function of time can be done using standard interaction data, or special data sets such as electron beam data and $-600 \text{ GeV}/c$ π^- beam data. For interaction data, the tracks need to be isolated so that one is not confused by nearby tracks or unassigned hits. In all data sets, in order to avoid bias in the results from using the RICH determination of the particle mass as much as possible, cuts from other detectors were applied. For $-600 \text{ GeV}/c$

beam data, the Beam Transition Radiation Detector (BTRD) was used to select π^- . For the electron beam data, both the BTRD and another TRD (ETRD) were used to select electrons. For interaction data, the momentum was limited to 100 GeV/c and below and the ETRD was used to eliminate electrons. Kaons and heavier mass particles were eliminated if these hypotheses from the likelihood analysis were selected as the most probable. All other tracks were kept and assigned the pion mass. Data on $(n - 1)$ versus time from interaction data, the electron beam data and a few randomly selected -600 GeV/c beam data is shown in Fig. 8. Two different estimates of the

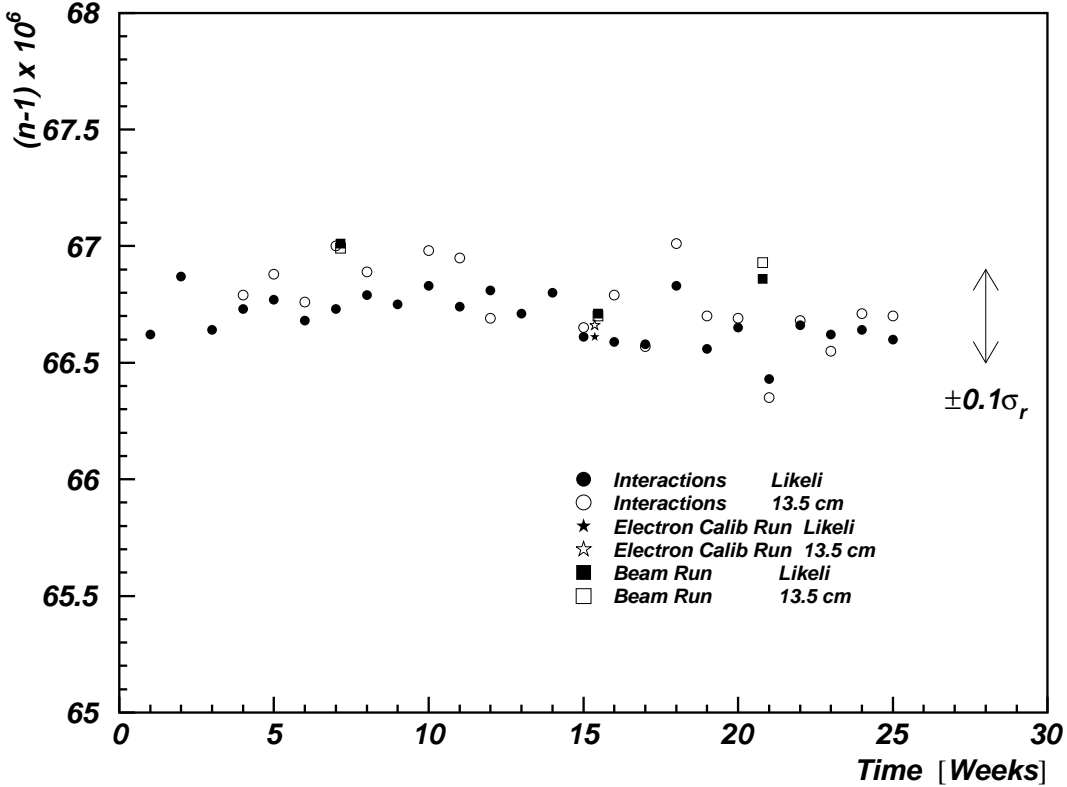


Fig. 8. $n - 1$ versus Time, determined with different methods, which are explained in the text. A $\pm 0.4 \cdot 10^{-6}$ change in $(n - 1)$ changes the ring radius only by 10% of the measured ring radius resolution σ_r .

ring radius were used to calculate $(n - 1)$. The first came from the Likelihood determination, using all hits within a $3\sigma_h$ cut²³ of the most probable radius. The second used all hits within 13.5 cm of the predicted track center. The second method does not rely on the likelihood analysis at all, but obviously has much more background. Shown on the figure is the range of $(n - 1)$ needed to change the central value of a $\beta = 1$ ring radius distribution by $\pm 0.1\sigma_r$. Here the ring radius resolution σ_r was taken to be 1.75 mm, the average of the isolated single track resolution and the value from the non-isolated track

²³ σ_h is the single hit resolution, determined in the next section.

study, as described later. As can be seen in the figure, the index of refraction of the gas was essentially constant over the entire run.

5.4 Determination of the single hit resolution σ_h

A basic parameter of the likelihood analysis is the single hit resolution. This is determined by histogramming the radial distance of all hits from a given track center which is determined by projected tracks from an upstream PWC system to the photocathode. The width of the resulting distribution is then the single hit resolution σ_h . Care has to be taken to select tracks that are of a similar kind, so that the distribution is not broadened by track-to-track differences such as momentum, particle type, etc. The data set used for this analysis was taken to calibrate another detector in the experiment (a lead glass detector), and consists of a set of 60 – 80 GeV/c single electron tracks (electron beam data) which populate the horizontal acceptance of the RICH. Because the electrons were well identified in two separate TRDs, there are no broadening effects for these $\beta = 1$ particles. The measured widths of the single hit radius distributions are summarized in table 2. The contribution

Track type	σ_h [mm]	
	Electron beam	Interaction
All tracks	5.40	5.75
All light on one mirror	5.25	5.67
All light from multiple mirrors	5.64	5.77

Table 2

RMS Widths of the single hit distance to ring center for different subclasses of tracks for electron beam and interaction data.

to this resolution from the finite precision of the mirror alignment procedure (σ_m) can be estimated from the quadratic difference of the resolution of radial distributions for tracks which had all of their light on a single mirror and for tracks which had their light distributed over more than one mirror, calculated from table 2 to be $\sigma_m = 2.06$ mm. The contribution to the single hit resolution from the finite precision of the PWC tracking system (σ_t) can be estimated by first fitting all of the found hits to a circle and then using the center of this circle (and not the predicted track center) to calculate the single hit resolution. The quadratic difference of this resolution, measured to be 4.81 mm, and that found by using the projected track is then a measure of the tracking system contribution, calculated to be $\sigma_t = 2.45$ mm (from chamber geometry, the expectation is $\sigma_t \approx 3.0$ mm).

A second data set, taken from interaction data, can also be used to measure the single hit resolution. For this data set, one needs to select a small momentum

range in which the radii for pion and kaon particles are well separated, here taken to be 60 – 65 GeV/c. Electrons were removed from the sample with a TRD cut. The resulting rms widths of the single hit radius distributions are shown in table 2. The single hit resolution measured from this data sample is $\sigma_h = 5.75$ mm. Because this data is restricted to a limited section of the phase space of the detector, for further analysis a single hit resolution from a weighted average of the two data sets of $\sigma_h = 5.5 \text{ mm} \pm 0.1 \text{ mm}$ is used. This can be compared to an estimate of this quantity calculated from the known physical parameters of the detector, given in Table 3.

Source	Value [mm]
Pixel Size (Spacing/4)	4.03
Mirror Alignment (σ_m)	2.06
PWC Resolution (σ_t)	3.0
Dispersion in Neon [13]	1.2
Total expected (σ_h)	5.54
Total measured (σ_h)	5.5 ± 0.1

Table 3
Contributions to the single hit resolution σ_h .

5.5 Determination of the ring radius resolution σ_r

Each phototube that fires gives an independent measurement of the ring radius, when the ring center is given by the measured track parameters. Thus the ring radius resolution σ_r should be given by

$$\sigma_r = \frac{\sigma_h}{\sqrt{N}} \quad (1)$$

where σ_h is the single hit resolution determined above, and N is the number of hits used for this ring. This can be measured in the electron beam data previously discussed. This is shown in table 4 which shows the rms widths for the ring radius distributions and the number of hits found on these rings for both a simple radius fit and for the Likelihood analysis output. For these distributions the single hit resolution of $\sigma_h = 5.5$ mm was used and a $3\sigma_h$ cut was applied to remove close noise hits. Using equation (1) above, one expects a ring radius resolution of $\sigma_r \approx 1.5$ mm, which is slightly larger than what is observed.

Measuring the single track ring radius resolution in this manner in interaction data is difficult because of the complication of overlapping tracks.

Method	N	σ_r [mm]	Expectation from equation (1) [mm]
Radial Fit	13.29	1.46	1.51 ± 0.03
Likelihood Fit	13.20	1.42	1.51 ± 0.03

Table 4

Number of hits and rms width of ring radius distributions for electron beam data.

Additional cuts have to be applied to isolate the tracks. Two cuts are applied: 1) the closest track must be at a distance of at least two electron radii away from the one considered and 2) the expected background from non-associated hits near the track considered must be no larger than 1. Again the single hit resolution was set to $\sigma_h = 5.5$ mm and a $3\sigma_h$ cut was used to constrain the number of hits assigned to tracks. When this is done, the resolution found is similar to that from single track events. This is shown in Fig. 9, which plots the ring radius distribution from 95 – 100 GeV/c isolated tracks. For these data, and for isolated 60 – 65 GeV/c pion tracks, the results are summarized in table 5. Here, the expectations from equa-

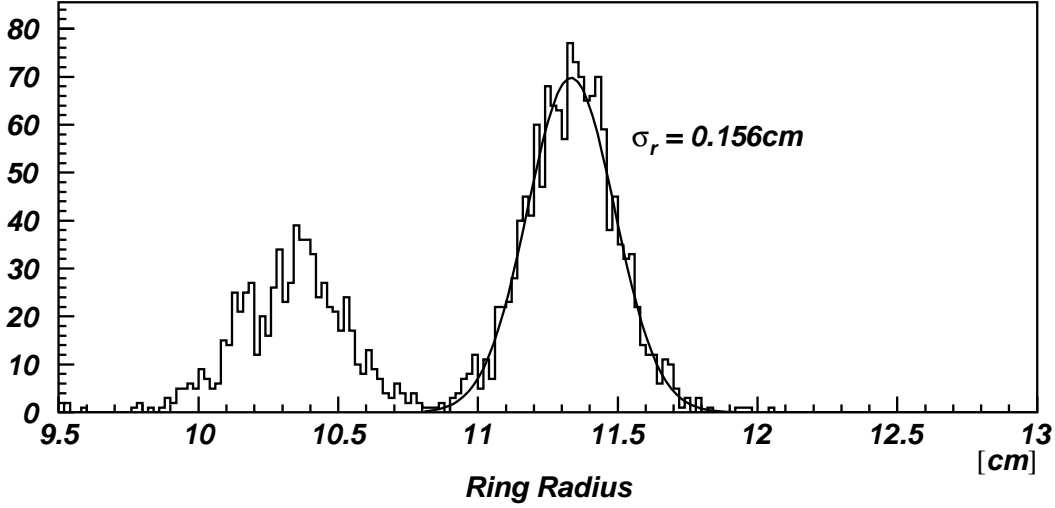


Fig. 9. Ring radius distributions for interaction data for tracks with 95 – 105 GeV/c momentum. Very well separated peaks corresponding to pions (right) and kaons (left) can be seen.

Momentum Range	N	σ_r [mm]	Expectation from equation (1) [mm]
95 – 105 GeV/c	13.18	1.56	1.51 ± 0.03
60 – 65 GeV/c	11.22	1.74	1.64 ± 0.03

Table 5

Number of hits and rms width of ring radius distributions for interaction data.

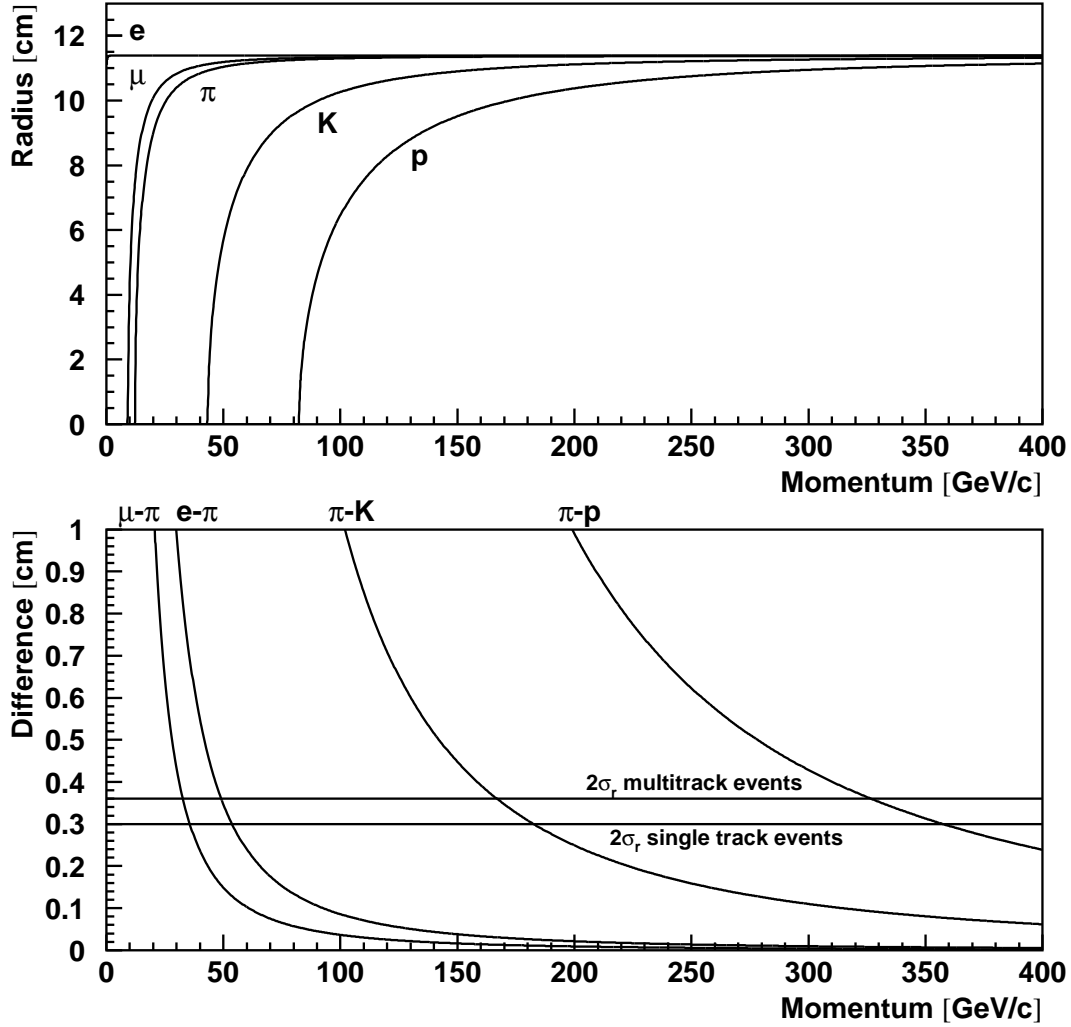


Fig. 10. Ring radii (top) and separation (bottom) for different particles. The two horizontal lines on the lower plot show the achieved resolutions for single track and multitrack events, respectively.

tion (1) are somewhat smaller than what is observed. Figure 10 shows the expected ring radii at the photodetector and the separation between different ring radii for various particle types as a function of momentum. A single track resolution of $\sigma_r = 1.5$ mm gives a $2\sigma_r$ π - K separation out to about 180 GeV/c.

6 Efficiencies for Particle Identification

To measure the efficiency for particle identification, a sample of $\Lambda \rightarrow p\pi^-$ decays was used, which can be reconstructed without using the information from the RICH detector, and determined how often the RICH identifies the

positive track as a proton. This study was performed in bins of 4 GeV/c in the proton momentum, and a total of 37000 Λ was used. For every momentum bin, the Λ peak was fit before and after a RICH cut²⁴ was applied to the positive track. In Fig. 11 it can be seen that the efficiency above the

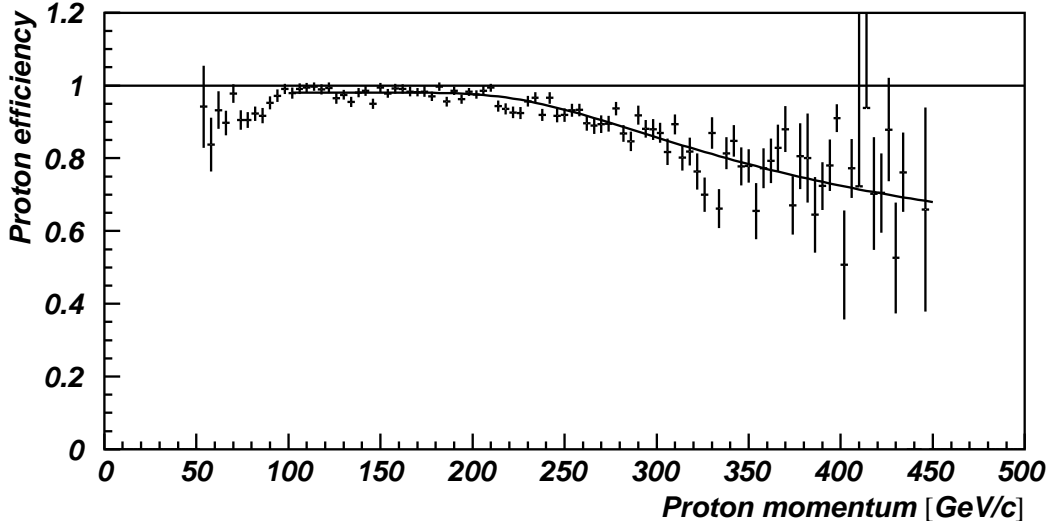


Fig. 11. Efficiency for identifying a proton as function of its momentum. The likelihood of the track to be a proton has to be at least as big as to be a pion.

proton threshold is well above 95%. Close to and below the proton threshold (≈ 90 GeV/c) the efficiency is slightly lower; in this region, the likelihood algorithm is very sensitive to fluctuations in the number of expected background hits. At higher momenta the proton and pion rings start to overlap. A fit which takes these overlaps into account (line in Fig. 11) gives a ring radius resolution of $\sigma_r = 1.8$ mm, which includes all effects such as overlapping rings from different tracks, tracking errors, etc, and because of these effects the ring radius resolution for multi-track events is larger than the ring radius resolution determined from isolated tracks. With the observed resolution it is possible to separate (on a $2\sigma_r$ level) kaons and pions up to 165 GeV/c and protons and pions up to 323 GeV/c. These numbers are expected to improve with ongoing work on the track reconstruction code, which should reduce the contribution of the PWC resolution (see table 3) to a negligible level.

Figure 12 shows the invariant mass for the two kaons in the reaction $\Sigma^- + A \rightarrow A + \Sigma^- K^+ K^-$. The event has exactly two negative and one positive outgoing tracks, and the energy of the outgoing particles is equal to the beam energy. A clear peak of the Φ can be seen, and the RICH identification has a very high efficiency for identifying the kaons. This confirms the proton result.

²⁴ Likelihood of the track to be a proton has to be at least as big as to be a pion.

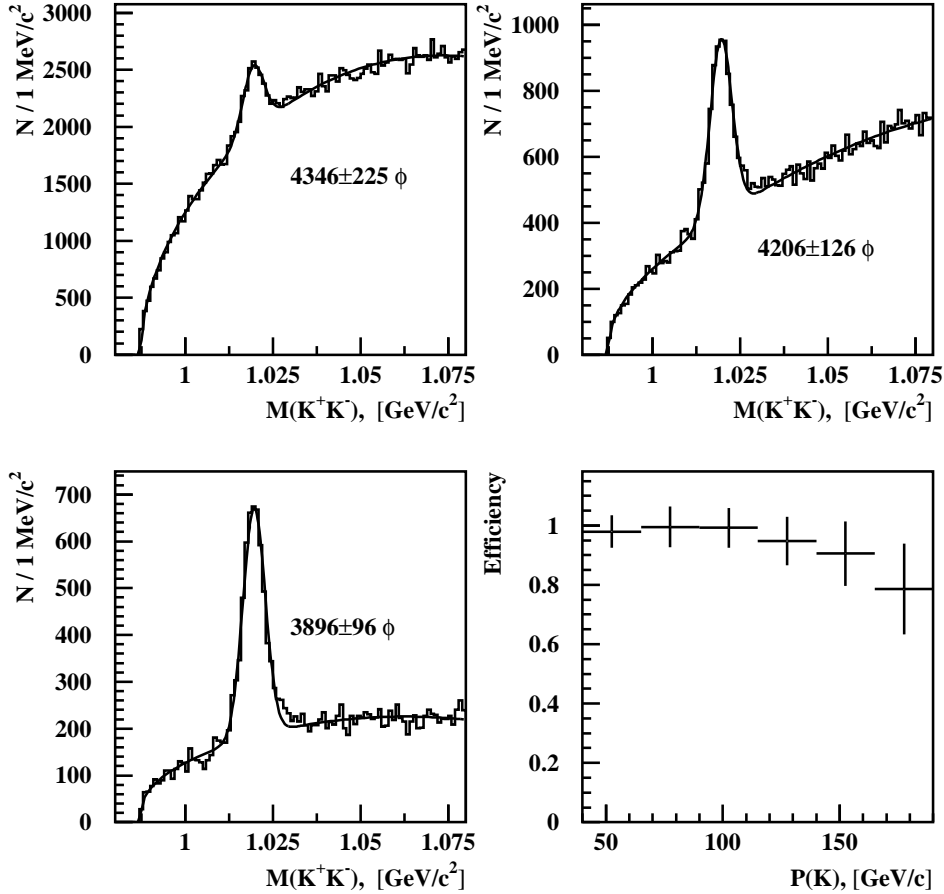


Fig. 12. Invariant mass of K^+K^- . Top left: No identification of the kaons. Top right: One kaon is identified. Bottom left: Both kaons identified. Bottom right: Efficiency for the RICH identifying a kaon as a function of its momentum. For identification, the likelihood of the track to be a kaon is required to be at least as big as to be a pion.

To measure the mis-identification rate, the Λ sample was used again, asking how often the π^- is identified as an antiproton or kaon, requiring that the likelihood of the track to be a pion is smaller than the maximum of the likelihoods to be a proton or kaon. The result can be seen in Fig. 13 to be only a few percent. For hypotheses below threshold the algorithm is sensitive to fluctuations in the background and to wrong ring center predictions by the track finding algorithm.

In Fig. 14 the use of the RICH detector in the charm data analysis of SELEX is demonstrated. The statistics available here is only a fraction of the experiment data (due to the high efficiency of the RICH detector, a particle identification

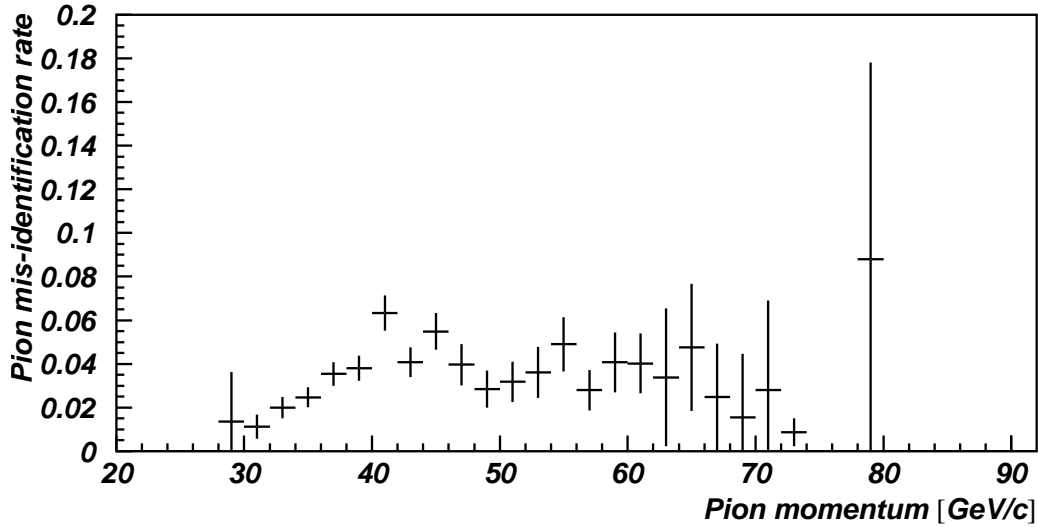


Fig. 13. Mis-identification rate (rate for identifying a pion as a proton or kaon) as a function of its momentum. The likelihood of the track to be a pion has to be smaller than the maximum of the likelihoods to be a proton or kaon.

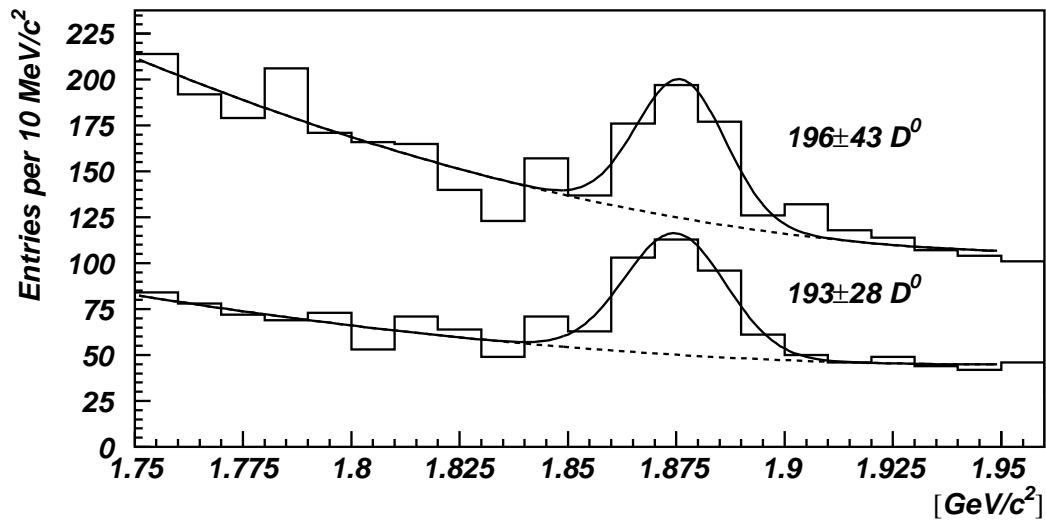


Fig. 14. Invariant mass of $K^- \pi^+$ (+cc) without and with RICH identified kaon. cut was used during most of the first stage processing of the data). A clear background suppression by a factor of 2.5 without a loss of signal (within the errors) is seen. This confirms the previous results that the RICH detector is very efficient.

7 Conclusions

In this article we described the construction and performance of the SELEX RICH detector. Stable performance of the detector was demonstrated over the 15 months of running time of the experiment. The refractive index did not change at all, and the Figure of Merit N_0 , which measures the efficiency of detecting photons, only varied slightly. It is on average for the central region 104 cm^{-1} , equivalent to 13.6 hits detected for a $\beta = 1$ particle.

The measured single hit resolution of $\sigma_h = 5.5 \text{ mm}$ can be explained totally by known factors and is dominated by the size of the phototubes; with ongoing work on the track reconstruction code, the second biggest contribution should be reduced significantly, and σ_h should approach 4.8 mm.

The ring radius resolution for isolated tracks can be explained totally by equation (1), and gives $\sigma_r = 1.5 \text{ mm}$. For interaction data, due to the overlapping of tracks, $\sigma_r = 1.8 \text{ mm}$ was obtained, which corresponds to about 1.6 % ring radius resolution at $\beta = 1$. This allows (on a $2\sigma_r$ level) the separation of kaons and pions up to 165 GeV/c and of protons and pions up to 323 GeV/c.

The efficiency of particle identification is very high ($\approx 98\%$) and only diminishes for high momenta as expected from the ring radius resolution. Below threshold, the efficiency is well above 90 %, with a mis-identification rate of only a few percent.

All the performance parameters of the SELEX RICH are as good or even better than projected from simulation and prototype tests [4]. The results from this detector are used as one of the key tools in the analysis of the SELEX data.

8 Acknowledgements

This work could not have been performed without the help of a lot of people. We would like to thank the engineering and technical support staffs at our institutes, especially at Fermilab, for their excellent work; V.I. Solyanik for his early contributions; our summer students; and the members of our collaboration and the Russian group leaders L.G. Landsberg and E.M. Leikin for their continuous encouragement and support.

References

- [1] SELEX Collaboration: Carnegie-Mellon University, Fermilab, University of Iowa, University of Rochester, University of Hawaii, University of Michigan-Flint, Ball State, Petersburg Nuclear Physics Institute, ITEP (Moscow), IHEP (Protvino), Moscow State University, University of São Paulo, Centro Brasileiro de Pesquisas Físicas (Rio de Janeiro), Universidade Federal da Paraíba, IHEP (Beijing), University of Bristol, Tel Aviv University, Max-Planck-Institut für Kernphysik (Heidelberg), University of Trieste, University of Rome “La Sapienza”, INFN, Universidad Autonoma de San Luis Potosí, Bogazici University.
- [2] Fermilab E781 SELEX Proposal, unpublished, and J. Russ, Nucl. Phys. **A585** (1995) 99.
- [3] A. Roberts, Nucl. Instr. and Meth. **9** (1960) 55.
- [4] M.P. Maia et al., Nucl. Instr. and Meth. **A326** (1993) 496
- [5] V.A. Dorofeev et al., Physics of Atomic Nuclei **57** (1994) 227.
- [6] J. Engelfried et al., Nucl. Instr. and Meth. **A409** (1998) 439
- [7] W.A. Campbell Jr. et al., NASA Reference Publication 1124, 1984.
- [8] R. Richardson and R. Schmitt, Adv. in Cryo. Eng. **41B** (1996) 1907.
- [9] E. Dambik, D. Kline, and R. West, “The Epicure Control System”, Proceedings of the International Conference on Accelerator and Large Experimental Physics Control Systems (ICALEPCS 93), Berlin, Germany, 18-22 Oct 1993. Fermilab-CONF-93-288
- [10] L. Stutte, J. Engelfried and J. Kilmer, Nucl. Instr. and Meth. **A369** (1996) 69.
- [11] A. Atamanchuk, V. Golovstov and L. Uvarov, “CROS - Coordinate Readout System for multiwire proportional chambers”, LNPI Research Report 1988-1989, Gatchina, 1990.
- [12] J. Séguinot and T. Ypsilantis, Nucl. Instr. and Meth. **142** (1977) 377.
- [13] A. Bideau-Mehu et al., J. Quant. Spectrosc. Radiat. Transfer **25** (1981) 395
- [14] U. Müller et al., Nucl. Instr. and Meth. **A343** (1994) 279.